Density functional theory calculations of thermodynamic and kinetic properties of point defects in β-U

David Andersson

Materials Science and Technology Division, Los Alamos National Laboratory, P.O. Box 1663, Los Alamos, NM, 87545, USA

Ben Beeler

Nuclear Materials, Computational Materials Science, North Carolina State University, Raleigh, NC, 27695, USA

Abstract

Density functional theory (DFT) calculations of the thermodynamic and kinetic properties of point defects in the β phase of uranium is reported. Defect energies and entropies were obtained using 2×2×2 supercells and the standard PBE exchange-correlation potential. Due to computational cost, calculations of the vibrational properties governing entropies were only performed for atoms within (roughly) the 3rd nearest neighbor shell of the defect. Migration barriers were estimated by nudged elastic band (NEB) calculations. The low symmetry of the β-U phase (the unit cell is tetragonal and contains 30 atoms) results in many point defect configurations and even more migration pathways. A connectivity map, starting from the most stable point defects, was developed in order to identify the rate-limiting step controlling the net diffusion rate in each crystallographic direction. The U self-diffusivity tensor was calculated by combining the defect formation energies, entropies and migration barriers. The fastest diffusion rate refers to a vacancy mechanism in the z direction and agrees well with experimental data on self-diffusion in the literature. The diffusion mechanisms identified in this study will inform fuel performance models of swelling and gas evolution.

Introduction

Metallic nuclear fuels are considered for application in several different reactor types, including micro-reactors and sodium-cooled fast reactors. Diffusion of point defects and fission gas atoms are important mechanisms for metal fuel micro-structure evolution under irradiation and impact several fuel performance metrics. Uranium metal fuel, which is often alloyed with other elements such as Zr, Mo and/or Pu, exhibits several different stable phases as function of the radial position in the fuel rod. This is a consequence of the redistribution of alloying elements and the temperature gradient across the fuel rod that occurs for in-pile conditions. For accurate prediction of swelling, fission gas release, and other related processes, the diffusion properties of point defects and fission atoms must be determined for each phase of uranium in the fuel. The present study focuses on point defect properties and the resulting self-diffusion behavior in the β phase of uranium under thermal equilibrium conditions, while future work plans to address Xe diffusion and the impact of irradiation. Before delving into the new results, the availability of experimental and computational

data for point defects and self-diffusion in the different phases of uranium are briefly reviewed, which emphasizes the need for additional computational data on the β phase in particular.

Self-diffusion in uranium has been investigated for the α-U [1], β-U [2] and γ-U [3] phases by isotope tracer diffusion experiments. The self-diffusivities differ by up to two orders of magnitude between the phases (from the β to the γ phase close to the transition temperature), even when the effect of temperature is accounted for by extrapolation, as highlighted in Figure 1. The diffusivity correlates with the complexity of the crystal structure, with the bcc γ-U phase having much higher diffusivity than the more complex α- and β-phases. Although there is experimental data for self-diffusion in all three uranium phases, simulations are able to provide additional information, for example, in the form of separate defect formation and migration properties, the sum of which makes up the experimentally measured activation energy for self-diffusion, and the diffusivity of competing mechanisms that may become important under irradiation. The formation and migration terms are needed separately in order to accurately model the irradiation response of the fuel. This and the need to validate methods for future studies of fission gas diffusion are the primary motivations for the present study. Formation energies can be measured independently of the activation energies by positron annihilation spectroscopy, which has been reported in [4] for the γ-U phase (although raw positron data was presented for all phases, the defect formation energy was only reported for the γ-U phase). The formation energies from positron annihilation spectroscopy can be used in combination with self-diffusion measurements of the activation energies to extract the migration barriers and thus enable direct comparison with the calculated values of the two separate contributions to the activation energy for self-diffusion. There are also other techniques to determine defect concentrations, e.g. dilatometry, and migration barriers, e.g. damage recovery experiments, but, to the best of our knowledge, no results have been reported using such techniques for uranium.

The bulk properties of the three main uranium phases have been studied using both density functional theory and empirical potentials [5-15]. The properties are generally well reproduced by the standard GGA methodology and the application of a Hubbard U model to treat strong correlations is not required for metallic uranium [10-12]. There are also computational investigations of the thermodynamic and kinetic properties of point defects. The formation and migration enthalpies (no entropies) of point defects in the α-U phase were studied using standard DFT calculations [5] and the calculated activation energy for diffusion agreed well with the experiments by Stelly and Servent and Adda et al. [2]. The γ-U phase has been investigated using both static DFT calculations [8,16] and ab initio molecular dynamics (AIMD) simulations [6]. Because γ-U is dynamically unstable at low temperatures, in order to avoid the lattice instability in calculations, either finite temperature ab initio molecular dynamics simulations have to be used, as in Ref. [6], or methods to stabilize the bcc lattice have to be introduced for the static 0 K DFT calculations [8,13-16]]. Ab initio molecular dynamics simulations constitute the most rigorous approach, but they are also computationally very expensive. The calculated and measured diffusivities for γ-U differ by one or two orders of magnitude depending on temperature and the activation energies are slightly different between theory and experiments. The calculated vacancy formation energy is in good agreement with that measured by positron annihilation spectroscopy [4], suggesting that the deviation originates from the migration energy. Similar to the study of point defects in α-U, entropy contributions were neglected for γ-U. However, this simplification is not believed to contribute to significant uncertainty in either case. The AIMD simulations were
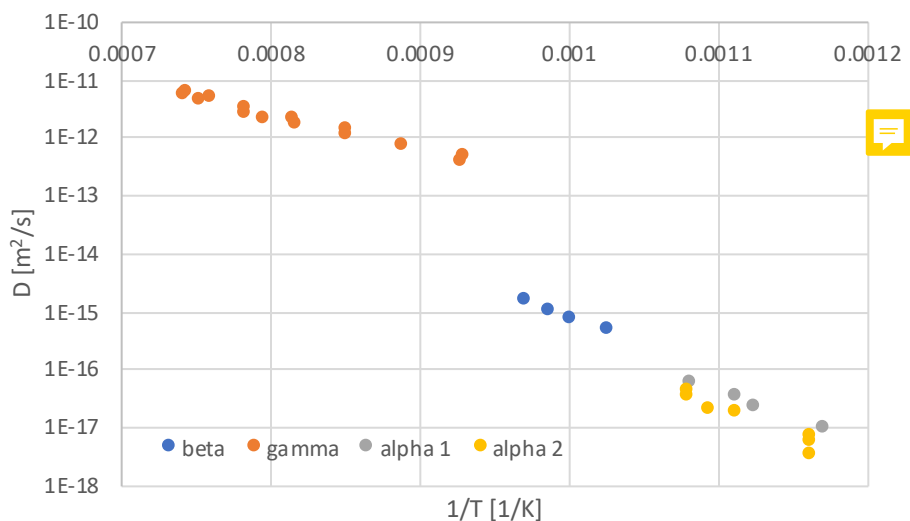
**Figure 1:** Collection of experimental data on self-diffusion in uranium phases as function of ~~temperature~~ (inverse temperature). The data points are from [3,17-23].

The β-U phase is stable in a narrow temperature range between the α-U and γ-U phases (943 K to 1048 K). There are a few computational studies of bulk β-U properties. ~~Lattice~~ parameters were predicted in fairly good agreement with experiments, although the high-temperature nature of the β-U phase complicates a one-to-one comparison with 0K DFT calculations [7,24]. Elastic constants were also calculated in [8], but, unfortunately, there is no experimental data to compare with. Extending beyond bulk properties to defects, ~~based on density functional theory (DFT) calculations,~~ the present study reports results for the point defect thermodynamic and kinetic properties in the β-U phase. ~~The results are compared to the experimental data referenced above.~~ The tetragonal unit cell of β-U has low symmetry and contains 30 atoms (see Figure 2) [25], which gives rise to many point defect possibilities and even more migration pathways for vacancies and interstitials. The defect energies are calculated for all unique crystallographic uranium vacancies and a long list of interstitial lattice locations. The results identify the lowest energy configurations. There are even more options for migration pathways of vacancies and interstitials. In order to obtain estimates of the effective diffusion rate in each crystallographic direction, a connectivity map starting from the most stable point defects was developed. The map was based on plausible pathways informed by the calculated migration barriers. ~~Additional work is still required and we envision extending the same methodology to fission gas properties.~~

This report is organized as follows. First, the DFT methodology and the models used for predicting defect concentrations and self-diffusivities are presented, ~~which is~~ followed by the corresponding results, comparison to experimental data and discussion. Finally, our summary and conclusions are presented together with an outlook for future work.
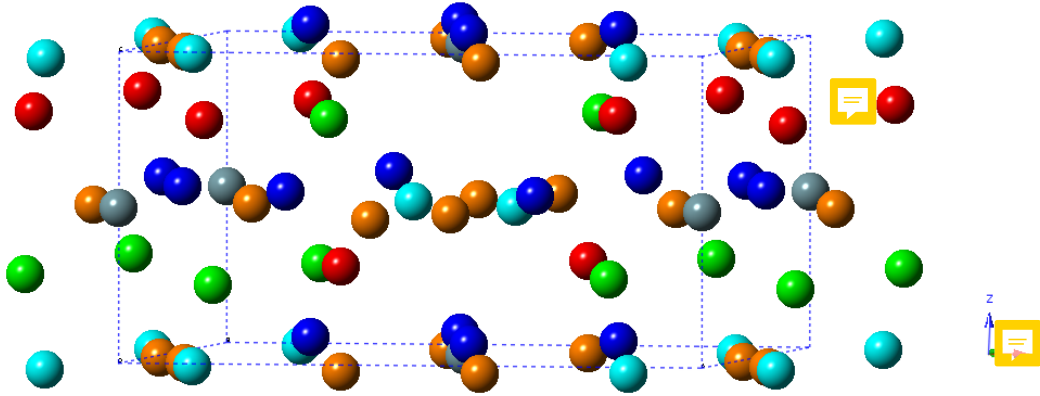
Figure 2: Unit cell of β-U with each unique crystallographic site (six) shown in different colors. Grey spheres correspond to the U1 position, turquoise to U2, green to U3, red to U4, blue to U5 and orange to U6. The supercells of β-U used in the present study are created by repeating this cell once in each crystallographic direction (2×2×2).

Computational methodology

DFT calculations

The point defect formation energies, entropies and migration barriers in the β-phase of uranium were calculated based on DFT using the VASP code [26-29]. Following the approach established in several existing DFT studies of uranium [12,30], the exchange correlation potential was described by the PBE parametrization without any Hubbard *U* parameter for the U 5f electron or spin-polarization, as those are not necessary to reproduce the properties of uranium. The predicted lattice parameters of the β-phase are consistent with experimental data, which was already reported by others [7,24], and summarized in Table 1. The discrepancies with regards to the a=b lattice parameters are at least partially related to thermal expansion (the experimental data is in the high-temperature region, more precisely 993 K, where the β phase is stable). This explanation may pertain to the internal parameters as well. The finite temperature behavior of the uranium lattice could be investigated by performing ab initio molecular dynamics simulations for β-U, but that is beyond the scope of the present study. Rather, it is assumed that the β-U description by DFT at 0K is sufficiently representative of the high-temperature structure to extract defect and diffusion parameters. This approximation is not believed to impact our main results or conclusions. The present work uses the β-U structure proposed by Donhoue [25] as the starting point, which is consistent with the conclusions in Ref. [24].

	A=b (Å)	c (Å)	U1	U2	U3	U4	U5	U6
Calc.	10.438	5.687	0.0	0.109	0.323	0.322	0.557	0.360
			0.0	0.109	0.323	0.322	0.223	0.048
			0.518	0.0497	0.738	0.284	0.032	0.019
Calc. [7]	10.454	5.634						
Calc. [24]	10.520	5.707						
Exp. [25]	10.759	5.656	0.0	0.107	0.303	0.321	0.558	0.372
			0.0	0.107	0.303	0.321	0.225	0.045
			0.5	-0.014	0.769	0.294	0.052	-0.023

Table 1: Calculated crystallographic data for the β-U phase compared experimental data [25] and DFT studies [7,24]. The columns for the U1, etc. (see Figure 3), positions represent fractional coordinates.

2×2×2 supercells were used to model the defect energies and migration barriers in the β-U phase, which contain 240 atoms. The atomic positions, supercell volume and supercell shape were allowed to fully relax (zero pressure on the cell and zero forces on the ions) in the energy minimization calculations. The calculations of migration barriers were performed at constant volume with the volume initially fixed at that of bulk β-U. For the rate-limiting step of the fastest diffusion mechanism, the results were further refined to include volume relaxation, see below for further details. The convergence criteria for the force relaxation was 0.01 eV/Å for all standard total energy calculations, but tighter convergence criteria (10^{-7} or 10^{-8} eV/Å) were applied for phonons. The plane-wave cut-off energy was set to 209.2 eV, which corresponds to the standard option for the accurate calculation setting in VASP. Convergence with respect to this parameter was verified for a few select defect properties. The total energy was calculated by integration in reciprocal space on 2×2×4 Monkhorst-Pack k-point meshes for the β-U 2×2×2 supercells and the partial occupancies were smeared according to the Methfessel-Paxton method with a smearing width of 0.1 eV. The convergence with respect to the k point mesh was also verified. The calculations for the β-U unit cell summarized in Table 1 used a 4×4×8 Monkhorst-Pack k-point, with all other setting the same as for the supercell calculations. The phonons calculations applied a reduced 1×1×2 k-point mesh for computational efficiency. The accuracy of this reduced mesh density will be verified to be sufficient for the most stable vacancy defect in future work, which will be assumed to extend to all other defects as well. At least within the accuracy currently sought for entropies.

Defect and diffusion models

Thermodynamic and kinetic properties of point defects are estimated by using the supercell data obtained from DFT calculations in thermodynamic and kinetic point defect model. The defect formation energies were calculated according to:

$$E_f(V_U) = E(V_U) - E(U)\frac{N-1}{N} \qquad (1)$$

$$E_f(U_i) = E(U_i) - E(U)\frac{N+1}{N} \qquad (2)$$

where $E_f(V_U)$ and $E_f(U_i)$ are the vacancy and interstitial defect formation energies, respectively, $E(V_U)$ and $E(U_i)$ are the energies of a supercell with one vacancy and interstitial, respectively, $E(U)$ is the energy of the perfect supercell and N is the number of atoms in the supercell.

Migration barriers were calculated using the nudged elastic band (NEB) method [30] with three images. The NEB calculations were performed with the volume fixed at that of bulk β-U. The diffusion mechanisms were identified by enumerating viable pathways, performing NEB calculations and then refining the pathways for cases where alternative options emerged. This approach is subject to the limitations of our ability to identify all important options and there is always a chance that a mechanism was missed. As such, the predicted diffusion coefficients represent a lower bound. For the rate-limiting step of the fastest diffusion mechanism, volume relaxation was performed with respect to the initial configuration and the climbing image version of the nudged elastic band method was used with five images. The change in the migration barrier was small, <0.02 eV, and consequently the fixed volume results without the climbing image method is considered sufficient for the purpose of screening viable diffusion pathways.

Defect formation entropies were calculated by assuming that the vibrational properties of atoms were only (significantly) influenced by the defects inside (roughly) the 3rd nearest neighbor shell or less, an approach which was tailored to reduce the computational cost associated with displacing all the ~240 atoms in the 2×2×2 supercell. For each point defect, the structure and the atoms included in the affected set are provided in the supplementary materials. In addition, Table 2 summarizes the number of atoms in the affected set for each defect.

	V_{U1}	V_{U2}	V_{U3}	V_{U4}	V_{U5}	V_{U6}
# in affected set	21	16	17	10	12	18
	U_{i1}	U_{i2}	U_{i3}	U_{i4}	U_{i5}	U_{i6}
# in affected set	17	13	19	19	23	14

Table 2: Number of atoms included in the affected set of atoms for each defect. The total number of atoms in the cell is 239 for vacancies and 241 for interstitials.

The equivalence of Eq. 1 and 2 for entropies applied to the (constrained) affected set of atoms read:

$$S_f(V_U) = \tilde{S}(V_U) - \tilde{S}(U) + \frac{S(U)}{N} \qquad (3)$$

$$S_f(U_i) = \tilde{S}(U_i) - \tilde{S}(U) - \frac{S(U)}{N} \qquad (4)$$

$S(U)$ is the entropy of the β-U supercell and N the number of atoms in the supercell. The perfect cell vibrational defect entropy was calculated from the normal mode phonon frequencies following the approach of Mishin et al. [31]. At temperatures higher than the Debye temperature, the entropy of crystalline solids can be approximated as:

$$S = -k_B \sum_{n=1}^{3N-3} ln\left(\frac{h\upsilon_n}{k_B T}\right) + (3N - 3)k_B \qquad (5)$$

Here, N is the number of atoms in the crystal, k_B is the Boltzmann constant, T is the temperature, and v_n is the normal vibrational frequency of the crystal. There are three modes that have imaginary frequencies for every supercell, corresponding to translational modes, which are neglected. The $\tilde{S}(V_U)$, $\tilde{S}(I_U)$ and $\tilde{S}(U)$ entropies are calculated using an equation similar to Eq. 5, but where the summation only covers the affected set of atoms for each case. The perfect cell summation adds the vacant site to the set for vacancies and the interstitial atom is removed for interstitials. In the harmonic approximation the temperature dependence in Eq. 5 cancels for the formation entropies in Eqs. (3) and (4).

The normal modes are calculated via the finite displacement method ~~finite displacement method~~ using VASP for the force calculations. Note that only the Γ point phonon frequencies are included in evaluation of the entropy.

The attempt frequency for migration, $v = v_0 exp\left(\frac{S_m}{k_B T}\right)$, can be calculated from the normal frequencies at the saddle point and at the initial configuration of the defect using the Vineyard method [32]:

$$v = \frac{\prod_{n=1}^{3N-3} v_n^{defect}}{\prod_{n=1}^{3N-4} v_n^{saddle}} \qquad (6)$$

N is the number of atoms and imaginary frequencies are not included in the summation (three translational modes for the defect and the same three translational modes for the saddle point with an extra imaginary mode inherent to the nature of the saddle point). ~~However, as~~ an approximation all attempt frequencies are initially set to 10^{13} s^{-1}, which is typically close to an upper bound for most materials. After identifying the rate-limiting step, the attempt frequency is calculated for that case following the approach involving a reduced set of affected atoms outlined above (only atoms in roughly the 3rd nearest neighbor shell are distorted in the phonon calculation). Frequencies arising from all other atoms are assumed to be the same for the initial configuration as for the saddle point, which is a necessary assumption to avoid excessive computational cost, while still allowing determination of frequencies with sufficient accuracy for the present purpose.

The pre-exponential factor for diffusion also includes factors related to the jump distance (d), number of available jump sites (Z), the correlation factor (f) and the dimensionality of the diffusion mechanism (D_z; 2 for 1D, 4 for 2D and 6 for 3D) according to

$$D_0 = \frac{1}{D_z} fZd^2v. \qquad (4)$$

The correlation factor is approximated as 1 in order to obtain an upper bound, which is slightly higher than the 0.781 value for the fcc lattice. d and Z are unique for each diffusion jump and will be specified for each mechanism in the results section.

The point defect diffusivities are obtained by combining the pre-exponential factor with the Arrhenius expression containing the migration barrier.

$$D = D_0 exp\left(-\frac{E_m}{k_BT}\right) \qquad\qquad (5)$$

The point defect diffusivities can be transformed to self-diffusivities by including the concentration of each defect. Here, those are approximated by the defect formation energy and entropy according to the dilute limit mass action law.

$$c = exp\left(\frac{S_f}{k_B}\right) \times exp\left(-\frac{H_f}{k_BT}\right) \qquad\qquad (6)$$

This expression refers to the fraction of defects on a particular crystallographic site and the overall concentration is obtained by weighting by the concentration of the particular site in question. This concentration is denoted $\tilde{c}$, which is currently approximated by multiplying the site fractions by 1/15. The U self-diffusivity is then obtained as

$$D_U = \tilde{c}D_0 exp\left(-\frac{E_m}{k_BT}\right). \qquad\qquad (7)$$

This equation refers to a particular diffusion mechanism and the total diffusivity would be calculated by summing up all contributions, however, if one mechanism is dominant, the total diffusivity can safely be approximated by this mechanism only. The diffusivity is a tensor property and each tensor component must be evaluated separately. The tetragonal crystal structure of β-U means that there are two distinct crystallographic diffusion rates, here labeled as the in-plane x-y diffusivity and the z axis diffusivity. The diffusivity in polycrystalline materials can then be estimated by using known bounds or performing meso-scale simulations of textures of interest. This exercise is beyond the present scope.
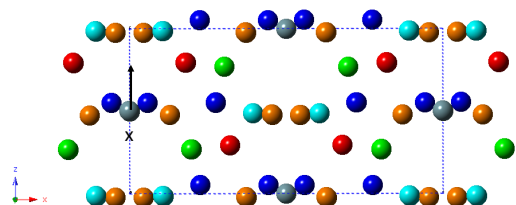
Results and discussion

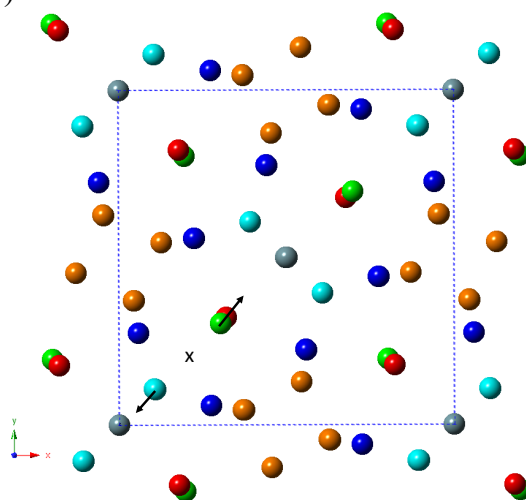*Vacancy and interstitial formation energies and entropies*
The calculated vacancy and interstitial formation energies and entropies are compiled in Table 3. The vacancy sites are labeled according to the uranium crystallographic site of the missing atom (V_{U1} for a vacant U1 site), see Figure 1, while the interstitial structures are shown in Figure 3. The defect concentrations obtained from the data in Table 3 using Eq. 6 are plotted in Figure 4. The vacancy of type 1 (V_{U1}) and interstitial of type 1 (U_{i1}) are shown to dominate across the entire temperature range relevant for the β-U phase. The stability of V_{U1} is driven by a high entropy contribution, since the formation energy of V_{U5} and V_{U6} are both lower than for V_{U1}. The high formation entropy may be related to the coordination environment, but further investigation is required to determine the cause.
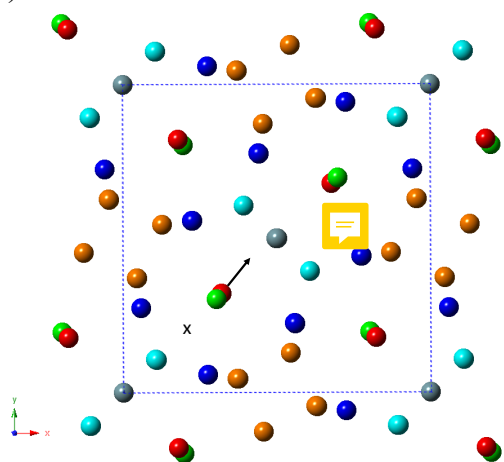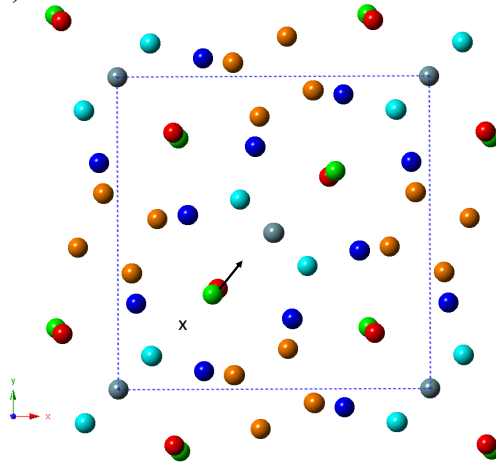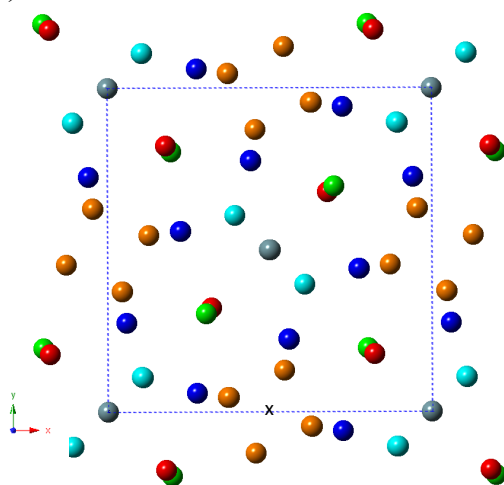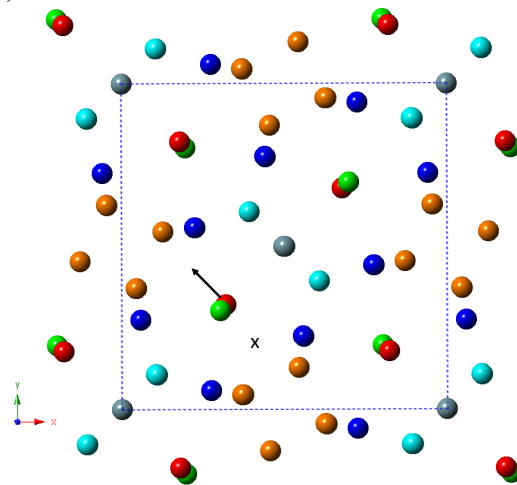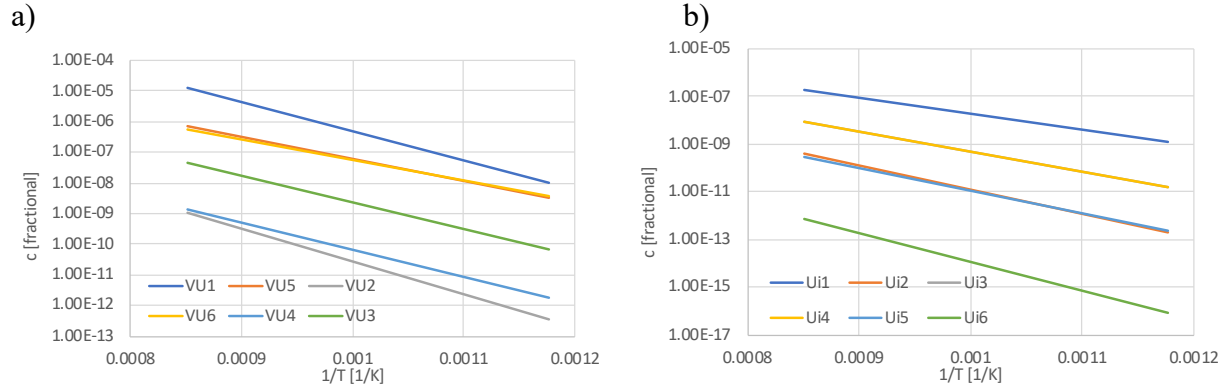
Figure 3: a)-f) illustrates the structures of interstitials 1 through 6 (U_{i1} through U_{i6}). Structure files are available in the supplementary materials. The interstitial atom is highlighted by 'x' and surrounding atoms that experience significant displacement (split structures) are shown by arrows.

a)

b)

Figure 4: Predicted concentrations of a) vacancies and b) interstitials in β-U.

The formation energies and entropies of the most favorable vacancy and interstitial are collected in Table 4, which also includes the calculated reference values for α-U [1] and γ-U [2]. For γ-U available experimental reference values are also reproduced. The vacancy formation energy is predicted to be higher in the β-U phase than in γ-U or α-U. This is a consequence of V_{U1} dominating over V_{U5} and V_{U6} due to entropy contributions. V_{U5} and V_{U6} have formation energies close to that predicted for the γ-U phase. The interstitial formation energy for the β-U phase is in-between that of the α-U and γ-U phases, with the latter being significantly higher. The lowest energy interstitial structure forms a split interstitial in the z direction. One of the vacancies (V_{U4}) and two of the interstitials have negative formation entropies (U_{i5} and U_{i6}). Negative formation entropies are not unphysical, but still somewhat unexpected and a sign of an unfavorable atomic coordination. None of the cases with negative formation entropies are very stable and further investigation of the origin is consequently curtailed. U_{i3} and U_{i4} relaxed to the same structure and are consequently assigned the same energy and entropy. Vacancies are predicted to be more abundant than interstitials in β-U.

	V_{U1}	V_{U2}	V_{U3}	V_{U4}	V_{U5}	V_{U6}
Energy (eV)	1.86	2.13	1.75	1.75	1.43	1.32
Entropy (k_b)	9.76	3.16	3.16	-0.28	2.71	1.34
	U_{i1}	U_{i2}	U_{i3}*	U_{i4}*	U_{i5}	U_{i6}
Energy (eV)	1.49	2.14	1.82	1.82	2.07	2.61
Entropy (k_b)	0.35	0.67	0.64	0.64	-0.49	-1.10

Table 3: Defect formation energies and entropies for vacancies and interstitials at different crystallographic sites in β-U ~~phases~~. The vacancy sites are based on the lattice location of uranium, see Figure 1, while the interstitial structures are shown in Figure 3. U_{i3} and U_{i4} (marked by an ~~asterix~~) relaxed to the same structure.

	H_f [eV] (U_i)	S_f [k_B] (U_i)	H_f [eV] (V_U)	S_f [k_B] (V_U)

α-U [5] (Calc.)	4.14	-	1.69	-
β-U [present work] (Calc.)	1.49	0.35	1.86	9.76
γ-U [6] (1000 K) (Calc.)	0.37	-	1.34	-
γ-U [4] (Exp.)	-	-	1.2±0.25	-

Table 4: Defect formation energies and entropies for vacancies and interstitials in uranium phases. Entropies are estimated from phonon calculations or not reported (labeled by '-'). The γ-U values are temperature dependent [6], but for the sake of simplicity we picked a fixed value at 1000 K for our analysis.

Defect migration mechanisms and migration barriers
Due to the low-symmetry of the β-U crystal structure, diffusion is complicated and net transport must inherently involve several steps. As an example, in order for a U1 vacancy to contribute to net diffusion, it must reach an equivalent site one lattice distance away, see Figure 5. This implies that it must jump through several other uranium sites. In order to estimate the effective migration barrier, the barriers of all intermediary steps and energies for each equilibrium lattice positions, must be calculated. The NEB technique used here to study migration barriers requires a priori definition of the starting and final position of the vacancy or interstitial. Moreover, in order to estimate the net diffusion rate, the highest migration barrier along a particular pathway must be identified. Among a range of different pathway options, the rate-controlling one will be that with the lowest effective migration barrier, however, just to re-iterate, it is the highest barrier along that pathway that ultimately controls the diffusion rate. The tetragonal crystal structure of β-U means that there are two distinct crystallographic diffusion rates, here labeled as the in-plane x-y diffusivity and the z axis diffusivity. Below the vacancy and interstitial diffusion mechanisms are reviewed and the relevant migration barriers reported.

Vacancy migration
The most probable in-plane and out-of-plane vacancy diffusion mechanisms are illustrated in Figure 5. Each step along the net diffusion pathways is shown with an arrow and the number next to it is the barrier in reference to the energy of a U1 vacancy. For in-plane x-y diffusion, the vacancy of type 1 is used as starting point, but any of the sites along a pathway could be considered as the starting position with the corresponding adjustment to the formation energy and migration barrier. The figure illustrates three main options for in-plane diffusion, with effective barriers ranging from 0.94 eV to 1.81 eV. There are additional permutations of the diffusion pathways shown in Figure 5, but they all reduce to the same effective barriers as those already shown. This implies that the effective barrier for diffusion in the x-y plane is 0.94 eV. The mechanism involves V_{U1}, V_{U2}, V_{U5}, V_{U6}, but sidesteps V_{U3} and V_{U4}. All the vacancy sites are covered by at least one of the three V_{U1} diffusion mechanisms. The enumeration in the figure suggests that all relevant pathways for x-y diffusion have been exhausted. Several additional calculations were performed in search of alternatives, but no transitions were found with barriers as low as those reported in Figure 6. Note that some of the x-y plane mechanisms also have a z component (see below).

The four main alternatives for vacancy diffusion along the z axis are shown in Figure 6. Other pathways exist, but were not included in the figure due to high barriers or the existence of more likely and shorter migration steps. The effective diffusion mechanisms have a low barrier of 0.27 eV and involves V_{U4} and V_{U6} sites. Other mechanisms have barriers that are similar to the x-y plane diffusion mechanisms.

a)   b)
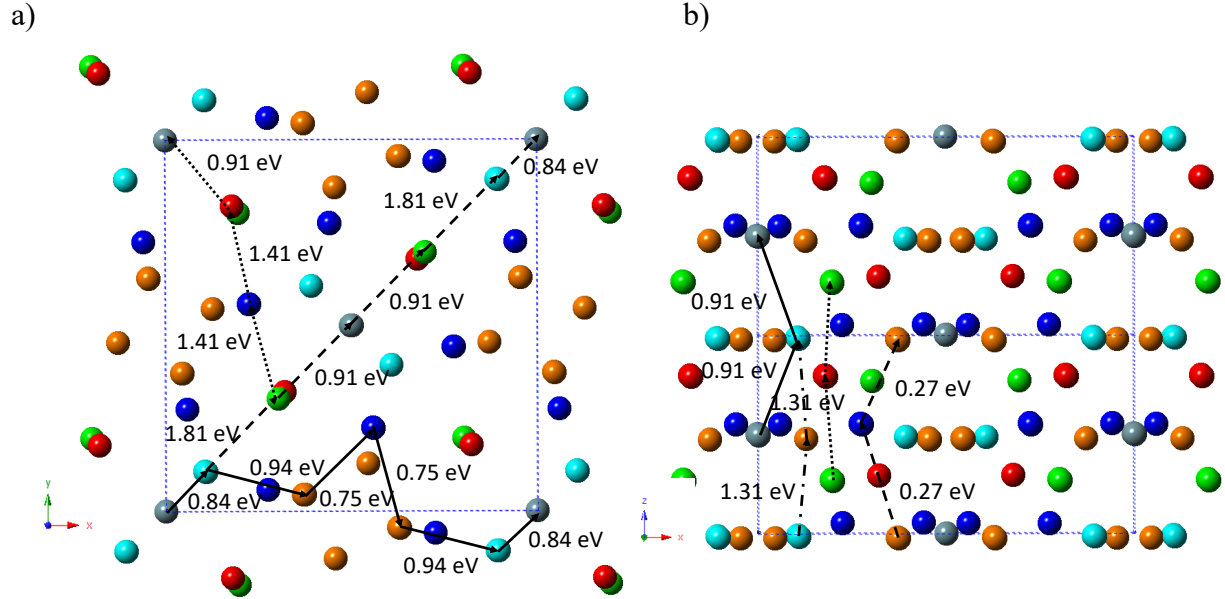
Figure 5: a) The net migration pathway for diffusion of type 1 vacancies in the x-y plane. Other vacancy types diffuse using the same mechanism. b) The net migration pathway for diffusion of type 1, 2, 3 and 6 vacancies along the z axis. In both figures, the start of the first arrow is meant to be a vacancy, which then follows the direction of the arrows. The atoms move in the direction opposite to the arrows.

U_{i1} is the most stable configuration. Diffusion in the x-y plane occurs according to the mechanism in Figure 6. U_{i1} forms a split structure along the z axis with a U1 atom. Any of the two split atoms may diffuse by an interstitialcy mechanism where a U2 atom is kicked out to form a split interstitial with a U3 or U4 atom. The barrier and energy of the final state for the split structure involving U3 or U4 atoms are identical for all practical purposes. The diffusion step is completed by the split structure involving the U3/U4 atoms moving into a position similar to the starting position of a split interstitial involving a U1 atom. This step does not involve a U2 atom as in the first migration step. Finally, net diffusion occurs by repeating the multi-step mechanism just described in either the same or reverse order to complete migration through the unit cell. The effective barrier for this diffusion mechanism is 0.75 eV and it refers to moving the first split interstitial structure to the split structure involving the U3/U4 atom by way of a U2 atom. The same mechanism may lead to diffusion along the z axis by changing the direction of some of the jumps along z axis, as also illustrated in Figure 6. The net diffusion barrier is the same as for diffusion in the x-y plane.
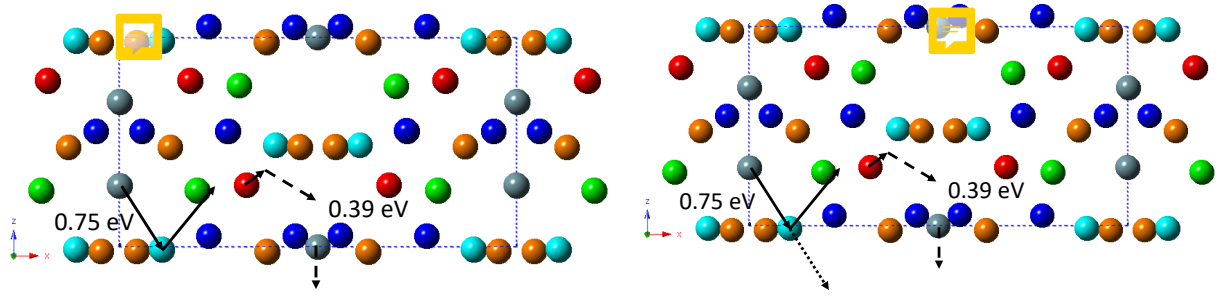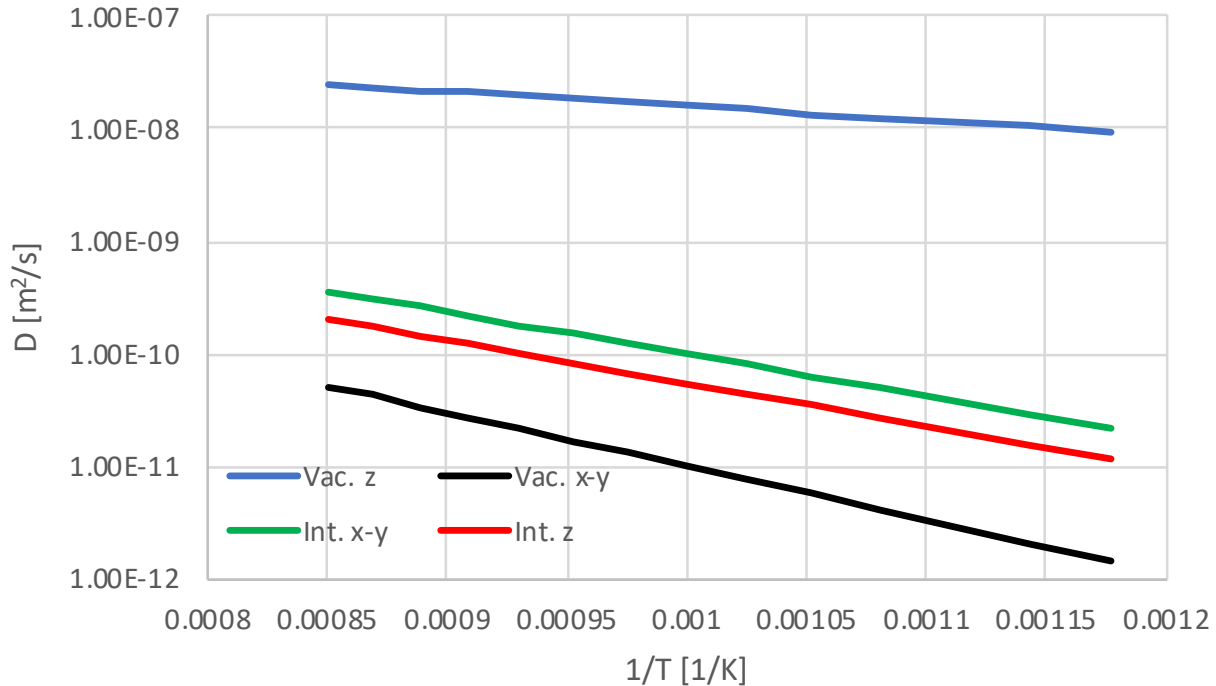
Figure 6: a) Interstitial diffusion in the x-y plane. b) Similar to a), but with the migration direction along the z axis changed for some steps such that net diffusion occurs along this axis. The difference compared a) is highlighted by the dotted arrow.

Point defect diffusion rates and self-diffusivities
The point defect diffusivities can be calculated from Eq. (5), with D_0 given by Eq. (4). D_z is 4 for diffusion in the x-y plane and 2 for diffusion along the z axis. d is given by the distances indicated in Figure 5 and 6. The correlation factor (f) is set to one and we use Z=4 for the x-y plane and 2 for the z axis. The fact that there are several pathways that can lead to net diffusion with a very similar effective migration barrier would lead to a revision of the multiplicity numbers, but such careful evaluation is left as future work (it will not significantly change the results). The vacancy and interstitial diffusion rates in the x-y plane and z direction are plotted in Figure 7 for the fastest mechanisms identified in Figures 5 and 6. All the rates are similar, with exception for vacancy diffusion in the z direction, which is almost two orders of magnitude higher.

Figure 7: Vacancy and interstitial diffusion rates in the x-y plane and along the z axis in β-U. All the rates are similar, with exception for vacancy diffusion in the z direction, which is almost two orders of magnitude higher.

The point defect diffusivities shown in Figure 7 are useful for analyzing radiation damage, since they control the rate of recombination and annihilation by sinks and thus the irradiation induced concentrations. However, they are not available through direct experimental measurements. The self-diffusivity for the interstitial and vacancy mechanisms are obtained by combining Eqs. (6) and (7). The results are plotted in Figure 8. This shows that vacancy diffusion in the z direction is the fastest mechanism for U self-diffusion. The diffusion rate for this mechanism agrees well with the experimental data due to Adda et al. [2]. The slope of the Arrhenius curve is slightly different between calculations and experiments (0.2 eV), which is still considered satisfactory agreement. The deviation from a linear relation in the experimental data points is sufficient to claim that the 0.2 eV is within the range of uncertainty. The attempt frequency in the pre-exponential factor was assumed to be 10^{13} s^{-1}. In order to verify the validity of this assumption, the attempt frequency was calculated using the methodology presented earlier to be [still running] s^{-1}. The corresponding diffusivity is also shown in Figure 8. The results confirm that the self-diffusivity in the β-U phase is lower than in the high-temperature γ-U [3] and low temperature α-U [1] phases (not shown in Figure 7).
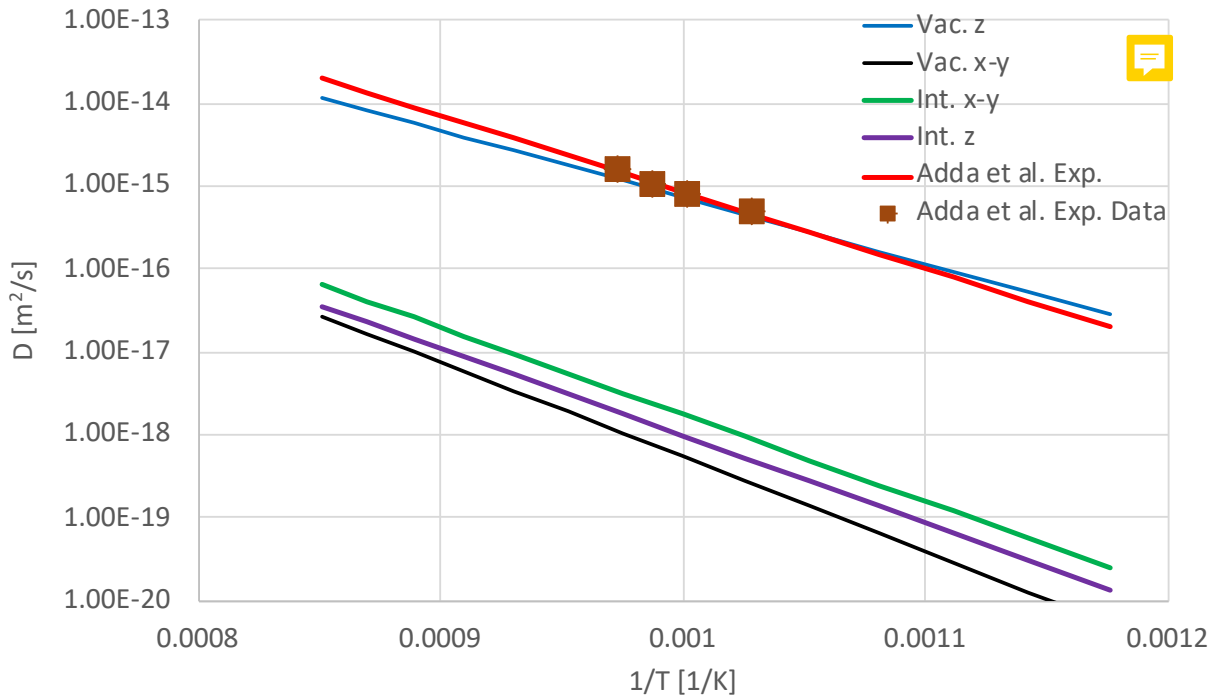
Figure 8: U self-diffusion rates in the x-y plane and along the z axis in β-U. All the rates are similar, with exception for vacancy diffusion in the z direction, which is at least one order of magnitude faster. The experimental data for β-U Adda et al. [2] is also included as reference.

Conclusions and outlook

The thermodynamic and kinetic properties of point defects in β-U were calculated from Density Functional Theory (DFT) calculations. The defect formation energies and entropies provide estimates of defect concentrations in thermal equilibrium, which predict the U1 vacancy to dominate. The stability of this vacancy is driven by a high formation entropy, while vacancies of

~~5 and 6~~ actually have lower formation ~~energies~~. Interstitials are lower in concentration than vacancies. The highest concentration ~~ease refers to~~ a split interstitial along the z axis involving the U1 atom. The fastest diffusion mechanism refers to a U6 vacancy in the z direction, which is several orders of magnitude faster than any of the other mechanisms. The predicted self-diffusivity for this mechanism agrees very well with available experimental self-diffusivities. These estimates can be ~~used by Bison developers for testing~~ in fuel performance simulations that resolve the individual phases of uranium as function of pellet radius. Next steps would include extending the calculations to include diffusion of the fission gas Xe and the fuel alloying element Zr.

References

[1] M. Stelly and J. M. Servant, J. Nucl. Mater. 43, 269 (1972).
[2] Y. Adda, A. Kirianenko and C. Mairy, J. Nucl. Mater. **3,** 300 (1969).
[3] Y. Adda and A. Kirianenko, J. Nucl. Mater. **2**, 120 (1959).
[4] H. Matter, J. Winter and W. Triftshauser, J. Nucl. Mater. **88**, 273 (1980).
[5] G.-Y. Huang and B. D. Wirth, J. Phys.: Condens. Matter **23**, 205402 (2011).
[6] B. Beeler, D. Andersson, C. Jiang, Y. Zhang, submitted (2020).
[7] B. Beeler, C. Deo, M. Baskes, M. Okuniewski, J. Nucl. Mater. **433**, 143 (2013).
[8] B. Beeler, B Good, S Rashkeev, z Deo, M Baskes, M Okuniewski, Journal of Physics: Condensed Matter **22**, 505703 (2010).
[9] B. Beeler, C Deo, M Baskes, M Okuniewski, Journal of Physics: Condensed Matter **24**, 075401 (2012).
[10] P. Söderlind, A. Landa, and P. E. A. Turchi, Phys. Rev. B **90**, 157101 (2014).
[11] W. Xie, W. Xiong, C. A. Marianetti, and D. Morgan, Phys. Rev. B **88**, 235128 (2013)
[12] P. Söderlind, Phys. Rev. B **66**, 085113 (2002).
[13] J. Bouchet and F. Bottin, Phys. Rev. B **95**, 154113 (2017)
[14] I. A. Kruglov, A. Yanilkin, A. R. Oganov and P. Korotaev, Phys. Rev. B **100**, 174104 (2019).
[15] A. Castellano, F. Bottin, B. Dorado and J. Bouchet, Phys. Rev. B **101**, 184111 (2020).
[16] B. Beeler, B. Good, S. Rashkeev, C. Deo, M. Baskes, and M. Okuniewski, J. Nucl. Mater. **425**, 2 (2012).
[17] A. A. Bochvar, V. G. Kuznetsova, V. S. Sergeev, F. P. Butra, Sov. Atom. Energy **18**, 761 (1965).
[18] S. J. Rothman, L. T. Lloyd, A.L. Harkness, Trans. AIME **218**, 605 (1960).
[19] Y. Adda, A. Kirianenko, C. Mairy, J. Nucl. Mater. **1**, 300 (1959).
[20] Y. Adda, A. Kirianenko, J. Nucl. Mater. **6**, 135 (1962).
[21] S. J. Rothman, J. Gray, J.P. Hughes, A.L. Harkness, J. Nucl. Mater. **3**, 72 (1961).
[22] S. J. Rothman, J.J. Hines, J. Gray, A.L. Harkness, J. Appl. Phys. **33**, 2113 (1962)
[23] S. J. Rothman, B. Bastar, J.J. Hines, D. Rokop, Trans. AIME **236**, 897 (1966).
[24] H. Li, Q. B. Ren, C. H. Lu, L. Lu, Y. Dai, B. X. Liu, J. Alloys Comp. **516**, 139 (2012).
[25] J. Donohue and H. Einspahr, Acta Cryst. B **27**, 1740 (1971).
[26] G. Kresse, J. Hafner, Phys. Rev. B **48**, 13115 (1993).
[27] G. Kresse, J. Furthmüller, Comput. Mater. Sci. **6**, 15 (1996).
[28] G. Kresse, J. Furthmüller, Phys. Rev. B **54**, 11169 (1996).
[29] J. P. Perdew, K. Burke and M. Ernzerhof, Phys. Rev. Lett. **77**, 3865 (1996).
[30] G. Henkelman, B. P. Uberuaga, H. Jonsson, J. Chem. Phys. **113**, 9901 (2000).
[31] Y. Mishin, M.R. Sorensen, A.F. Voter, Phil. Mag. **81**, 2591 (2001).